LETTER

doi:10.1038/nature12582

Exploiting dimensionality and defect mitigation to create tunable microwave dielectrics

Che-Hui Lee[1,2]*, Nathan D. Orloff[3,4]*, Turan Birol[5]*, Ye Zhu[5], Veronica Goian[6], Eduard Rocas[7], Ryan Haislmaier[2], Eftihia Vlahos[2], Julia A. Mundy[5], Lena F. Kourkoutis[5,8], Yuefeng Nie[1], Michael D. Biegalski[9], Jingshu Zhang[1], Margitta Bernhagen[10], Nicole A. Benedek[11], Yongsam Kim[5], Joel D. Brock[5], Reinhard Uecker[10], X. X. Xi[12], Venkatraman Gopalan[2], Dmitry Nuzhnyy[6], Stanislav Kamba[6], David A. Muller[5,8], Ichiro Takeuchi[13], James C. Booth[3], Craig J. Fennie[5] & Darrell G. Schlom[1,8]

The miniaturization and integration of frequency-agile microwave circuits—relevant to electronically tunable filters, antennas, resonators and phase shifters—with microelectronics offers tantalizing device possibilities, yet requires thin films whose dielectric constant at gigahertz frequencies can be tuned by applying a quasi-static electric field[1]. Appropriate systems such as $Ba_xSr_{1-x}TiO_3$ have a paraelectric–ferroelectric transition just below ambient temperature, providing high tunability[1–3]. Unfortunately, such films suffer significant losses arising from defects. Recognizing that progress is stymied by dielectric loss, we start with a system with exceptionally low loss—$Sr_{n+1}Ti_nO_{3n+1}$ phases[4,5]—in which $(SrO)_2$ crystallographic shear[6,7] planes provide an alternative to the formation of point defects for accommodating non-stoichiometry[8,9]. Here we report the experimental realization of a highly tunable ground state arising from the emergence of a local ferroelectric instability[10] in biaxially strained $Sr_{n+1}Ti_nO_{3n+1}$ phases with $n \geq 3$ at frequencies up to 125 GHz. In contrast to traditional methods of modifying ferroelectrics—doping[1–3,11,12] or strain[13–16]—in this unique system an increase in the separation between the $(SrO)_2$ planes, which can be achieved by changing n, bolsters the local ferroelectric instability. This new control parameter, n, can be exploited to achieve a figure of merit at room temperature that rivals all known tunable microwave dielectrics[3].

Ferroelectric thin films possessing a nonlinear dielectric response to a quasi-static electric field have been widely pursued for tunable dielectric devices[17–20] that work at gigahertz frequencies. $Ba_xSr_{1-x}TiO_3$ is the most common of such materials because of its high tunability ($\Delta K/K$, where K is the dielectric constant and ΔK is the change in dielectric constant under the application of a quasi-static electric field) and composition-dependent Curie temperature, T_C (refs 1–3, 11, 12). Thin films, however, of $Ba_xSr_{1-x}TiO_3$ suffer significant dielectric losses at application-relevant operating frequencies[1,12,21]. These losses are believed to arise from the motion of charged defects in a time-dependent electromagnetic field, as well as local polar nanoregions induced by structural imperfections and non-stoichiometry[1]. These losses are significantly higher in $Ba_xSr_{1-x}TiO_3$ films than in the bulk material[1,21].

Our approach to this problem is to take a system with low loss related to $Ba_xSr_{1-x}TiO_3$, and engineer it to improve its tunability. We selected the $Sr_{n+1}Ti_nO_{3n+1}$ Ruddlesden–Popper series of phases[22,23], which are known to have low loss in bulk[4,5]. In this homologous series, the positive integer n corresponds to the number of perovskite $SrTiO_3$ layers that are sandwiched between double SrO rock-salt layers (Fig. 1a). Although bulk $Sr_{n+1}Ti_nO_{3n+1}$ phases are centrosymmetric[22,23] and are thus non-polar, calculations from first principles recently predicted that under biaxial tensile strain $Sr_{n+1}Ti_nO_{3n+1}$ phases can exhibit a ferroelectric instability[24], local to the perovskite layers, if the spacing between the $(SrO)_2$ planes is sufficiently large (high n) to exceed a coherence length that depends on epitaxial strain[10].

In Fig. 1b (right-hand axis), the square of the in-plane polar phonon frequencies of $Sr_{n+1}Ti_nO_{3n+1}$ phases, calculated from first principles, are plotted as a function of n for $Sr_{n+1}Ti_nO_{3n+1}$ commensurately strained to the in-plane lattice parameter of a (110) $DyScO_3$ substrate. (Details of the calculations are provided in ref. 10 and in Methods.) It is seen that there is a critical n_c at which the square of the polar soft-mode frequency becomes negative, indicating a ferroelectric instability, and ferroelectricity for $n \geq n_c$ is expected. This n_c can also be seen from the energy lowering provided by the local ferroelectric instability (Fig. 1b, left-hand axis) and the curves of energy against total in-plane polar displacement in the $Sr_{n+1}Ti_nO_{3n+1}$ (Fig. 1c, d). Our calculations show that for $n \geq 3$ a local ferroelectric instability is expected at $T = 0$ for $Sr_{n+1}Ti_nO_{3n+1}$ commensurate with (110) $DyScO_3$. (The instability at $n = 2$ is too weak to stabilize a spontaneous polarization when quantum fluctuations of nuclei are considered[10].) As Fig. 1b–d shows, the in-plane ferroelectric instability of $Sr_{n+1}Ti_nO_{3n+1}$ phases can be tuned by changing the out-of-plane distance between the $(SrO)_2$ layers; that is, by changing the value of n. Such a control parameter is a new[10] and potentially disorder-free way of manipulating the properties of a tunable dielectric.

Recognizing that the presence of $(SrO)_2$ crystallographic shear planes[6,7] in $Sr_{n+1}Ti_nO_{3n+1}$ phases with finite n could provide a means of locally accommodating non-stoichiometry[8,9] (as described below), we investigate the tunable dielectric figure of merit[25] (FOM)

$$\frac{K(V=0)-K(V)}{K(V=0)\tan\delta}$$

of commensurate $Sr_{n+1}Ti_nO_{3n+1}$ films grown on (110) $DyScO_3$ with finite $n > n_c$. Although the $n = 1, 2, 3$ and $n = \infty$ members of the $Sr_{n+1}Ti_nO_{3n+1}$ series are the only compositions that can be synthesized in single-phase form in bulk material[9,22,23], by supplying incident species in an ordered sequence with submonolayer composition control, oxide molecular-beam epitaxy has enabled the growth of $Sr_{n+1}Ti_nO_{3n+1}$ films with n as high as 10 in single-phase form[26], even though the formation energies of high-n phases are essentially degenerate[27,28].

In this study we grew epitaxial $n = 1$ to $n = 6$ $Sr_{n+1}Ti_nO_{3n+1}$ films on (110) $DyScO_3$ and (110) $GdScO_3$ substrates[29]. (Details of the thin-film growth are given in Methods.) X-ray diffraction (XRD) scans (Fig. 2a and Extended Data Figs 2–4) of the $n = 1$ to $n = 6$ films reveal them to

[1]Department of Materials Science and Engineering, Cornell University, Ithaca, New York 14853, USA. [2]Department of Materials Science and Engineering, Pennsylvania State University, University Park, Pennsylvania 16802, USA. [3]National Institute of Standards and Technology, Boulder, Colorado 80305, USA. [4]Department of Physics, University of Maryland, College Park, Maryland 20742, USA. [5]School of Applied and Engineering Physics, Cornell University, Ithaca, New York 14853, USA. [6]Institute of Physics ASCR, Na Slovance 2, 182 21 Prague 8, Czech Republic. [7]Department of Signal Theory and Communications, Universitat Politècnica de Catalunya, 08034 Barcelona, Spain. [8]Kavli Institute at Cornell for Nanoscale Science, Ithaca, New York 14853, USA. [9]Center for Nanophase Materials Sciences, Oak Ridge National Laboratory, Oak Ridge, Tennessee 37831, USA. [10]Leibniz Institute for Crystal Growth, Max-Born-Strasse 2, D-12489 Berlin, Germany. [11]Materials Science and Engineering Program, The University of Texas at Austin, Austin, Texas 78712, USA. [12]Department of Physics, Temple University, Philadelphia, Pennsylvania 19122, USA. [13]Department of Materials Science and Engineering, University of Maryland, College Park, Maryland 20742, USA.
*These authors contributed equally to this work.

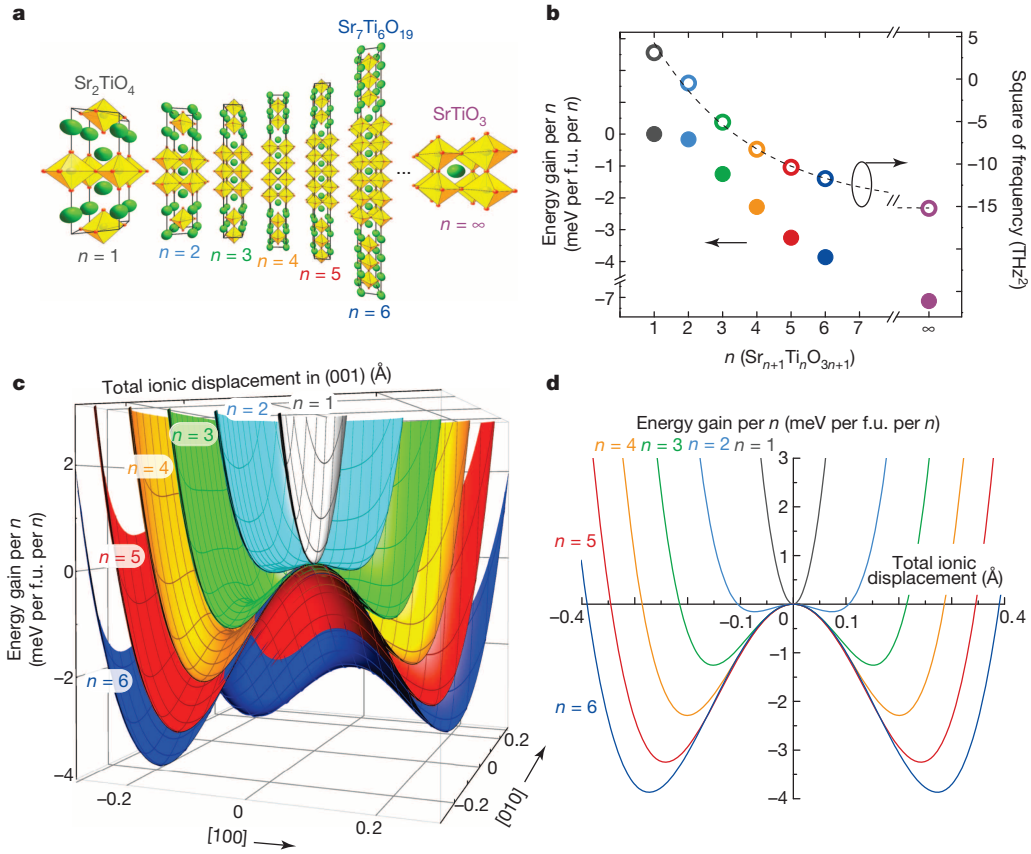

Figure 1 | First-principles calculations showing how the index *n* of $Sr_{n+1}Ti_nO_{3n+1}$ phases strained commensurately to (110) $DyScO_3$ substrates can be used to control the local ferroelectric instability. **a**, Diagram of the crystal structure of a unit cell of the $n = 1$–6 and $n = \infty$ members of the $Sr_{n+1}Ti_nO_{3n+1}$ phases. **b**, Square of polar soft-phonon-mode frequency (right-hand axis) and the energy gain per *n* (left-hand axis) of the ferroelectric state with respect to the nonpolar state, calculated from first principles. Energy gains are calculated by performing ionic relaxations under boundary conditions of fixed biaxial strain. F.u., formula unit. **c**, Energy (per *n*) with respect to the nonpolar state of $Sr_{n+1}Ti_nO_{3n+1}$ phases for polar distortions in the (001) plane. The distortion pattern is obtained from the ionic relaxations for larger values of *n*, and from the force constants matrix for smaller values of *n* (Methods). **d**, Cut of energy surfaces in **c** for polarization along the [110] axis.

be single-phase and commensurately strained to the substrates on which they were grown. The θ–2θ XRD scan of each $Sr_{n+1}Ti_nO_{3n+1}$ film shows all expected peaks and seems to imply perfect layer periodicity along the out-of-plane direction in each sample. Bright-field scanning transmission electron microscope (STEM) images of the $n = 6/DyScO_3$ sample (Fig. 2b), however, show that there are not only periodic horizontal $(SrO)_2$ planes but also aperiodic vertical $(SrO)_2$ planes. A histogram analysis (Fig. 2c) of the layering disorder reveals that most of the layers along the growth direction are composed of the desired six perovskite layers. The remaining layers have spacings that are harmonics of $n = 6$—that is, locally $n = 12$, 18 and 24—that are well lattice-matched to the surrounding $n = 6$ matrix. These harmonic *n* values and vertical $(SrO)_2$ layers probably form to accommodate local stoichiometry variations encountered during growth[8,9]. Atomic models of the $n = 6$ phase illustrating its ability to accommodate local non-stoichiometry are provided in Fig. 2d–g.

The dielectric properties of $Sr_{n+1}Ti_nO_{3n+1}$ samples were measured over a frequency range of 1 kHz to 125 GHz with a broadband, on-wafer technique[21]. The temperature dependence of the real part of the in-plane dielectric constant, $K_{11}(T)$, in the low-frequency regime (from 10 kHz to 1 MHz) is shown in Fig. 3a. The strong peak in $K_{11}(T)$, for $Sr_{n+1}Ti_nO_{3n+1}$ films with $n \geq 3$, is indicative of a phase transition from a paraelectric state above the transition temperature (T_C) to a state with local ferroelectric order below T_C, in agreement with theory (Fig. 1b–d).

The relationship between T_C and *n* determined from $K_{11}(T)$ measurements on films subjected to two different strain states by growth on $DyScO_3$ and $GdScO_3$ substrates is shown in Fig. 3b. T_C of the $Sr_{n+1}Ti_nO_{3n+1}$ ($n = 3$–$6, \infty$) phases on both substrates systematically increases with *n*, as expected from theory (second-harmonic generation (SHG) shows the same trend in T_C; Extended Data Fig. 5). Also consistent is the higher T_C observed on $GdScO_3$ as a result of the larger strain. Figure 3c shows the dependence of the spontaneous polarization measured at 10 K on *n* for the films deposited on $DyScO_3$.

Because the dielectric properties at room temperature are particularly important for applications, we examine the $n = 6/DyScO_3$ sample in detail at 300 K. Figure 4a shows the real and imaginary parts of the in-plane dielectric constant measured from 1 kHz to 125 GHz, demonstrating low loss and dispersionless response over almost the entire radiofrequency and microwave range. Even at ~1 THz, K_{11} remains unchanged (Methods), showing that phonons are the predominant contributor to K_{11} at 300 K over this broad frequency range. The inset to Fig. 4a shows the loss tangent of the same film on a linear frequency scale, indicating that only at the highest measurement frequencies does the loss become appreciable. Figure 4b shows the tunability at room temperature, indicating roughly 20% film tuning for a bias field of 50 kV cm^{-1} across the entire microwave range. On the basis of a model of the frequency dependence of the loss (Methods), we fit this loss tangent to a linear frequency dependence and calculate the film quality factor ($Q = 1/\tan\delta$), plotted in Fig. 4c. Also shown as solid symbols in Fig. 4c is the film *Q*, calculated by averaging the loss tangent data over a frequency window of width ~14.5 GHz. We then determine the film's FOM by multiplying the film *Q* by the relative tuning of 20%, obtaining the result shown in red in Fig. 4c. For comparison we also plot in Fig. 4c the best reliable report of the FOM of a $Ba_xSr_{1-x}TiO_3$ film at room temperature[30]. Even though the FOM of the $Ba_xSr_{1-x}TiO_3$ film is measured at a bias field sixfold higher, the $n = 6/DyScO_3$ sample

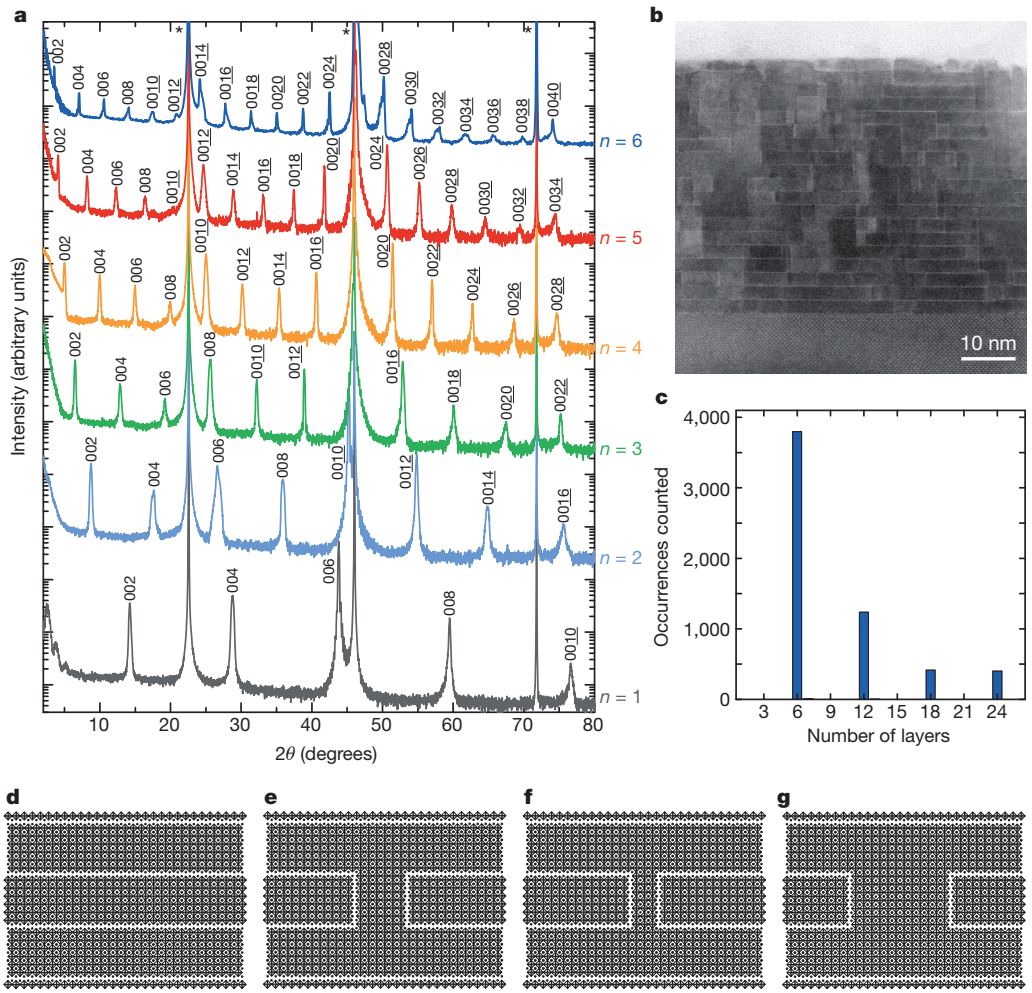

Figure 2 | Structural characterization by XRD and TEM. **a**, θ–2θ scans of epitaxial $Sr_{n+1}Ti_nO_{3n+1}$ (n = 1–6) films grown on (110) $DyScO_3$. Substrate peaks are labelled with an asterisk, and the plots are offset for clarity. **b**, Bright-field STEM image of the n = 6 film grown on $DyScO_3$. **c**, Histogram of the number of perovskite layers between $(SrO)_2$ layers along the out-of-plane direction. **d**, Schematic two-dimensional atomic representation of the strontium atoms and TiO_6 octrahedra of the ideal, stoichiometric n = 6 phase. **e**, When vertical $(SrO)_2$ layers are introduced, their overall density determines the SrO content of the film. This content is proportional to the length of the $(SrO)_2$ crystallographic shear planes, which show up as white lines in this two-dimensional diagram. For the case drawn, the stoichiometry is the same as in **d**. **f**, **g**, Local non-stoichiometry accommodation is shown for the case of regions that are ~7% Sr-rich (**f**) and ~12% Sr-poor (**g**).

shows a significantly better FOM over the entire microwave frequency range, achieving a value of ~50 at 10 GHz. This n = 6 sample has a higher FOM than any known electronically tunable dielectric at room temperature and comparable electric field.

The temperature dependence of the broadband frequency-dependent dielectric constant function of the n = 6/$DyScO_3$ sample allows us to conclude that losses in this material are almost entirely due to polar nanoregions that have a finite distribution of sizes (Methods). These

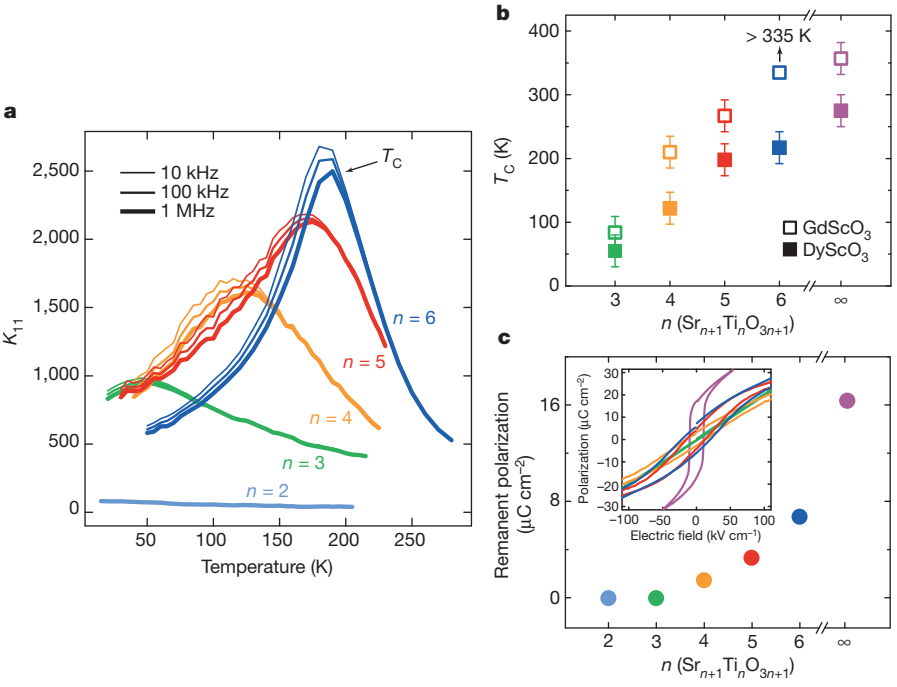

Figure 3 | Emergence of ferroelectricity in $Sr_{n+1}Ti_nO_{3n+1}$ films grown on (110) $DyScO_3$ and (110) $GdScO_3$. **a**, Temperature dependence of the real part of the in-plane dielectric constant (K_{11}) of n = 2–6 films deposited on (110) $DyScO_3$ at 10 kHz, 100 kHz and 1 MHz. **b**, T_C as a function of n for the n = 3–6 and $n = \infty$ films on (110) $DyScO_3$ and (110) $GdScO_3$. T_C is taken to be the temperature at which K_{11} is greatest at a measurement frequency of 1 MHz. T_C of the n = 6/$DyScO_3$ sample is indicated in **a**. The error bars correspond to the average variation of T_C among separately grown and measured samples having duplicate n values. The samples grown on $DyScO_3$ had duplicates, but not the samples on $GdScO_3$. **c**, Remanent polarization at 10 K as a function of n for the n = 2–6 and $n = \infty$ films on (110) $DyScO_3$. The inset is a plot of polarization against electric field hysteresis loops measured at 10 K. The bright-field TEM image and the θ–2θ rocking curve XRD scans from the same n = 6 sample characterized in **a** are shown in Fig. 2b and Extended Data Fig. 3a, respectively.

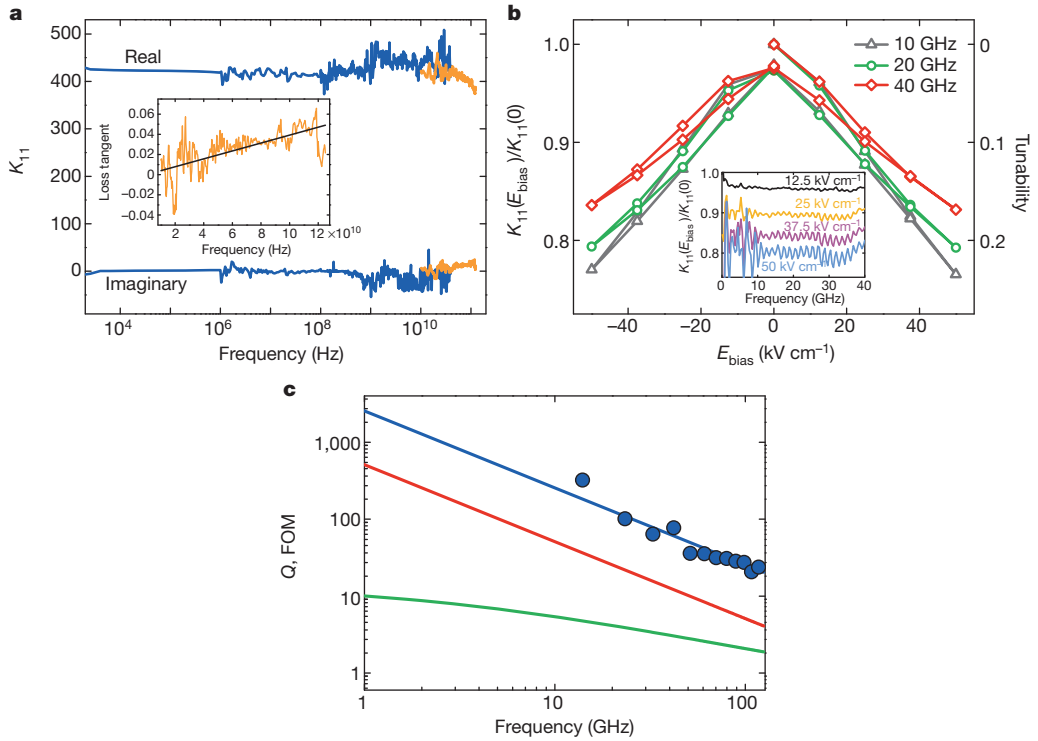

Figure 4 | In-plane dielectric constant (K_{11}) of $n = 6$ film on (110) $DyScO_3$, and its tunability at room temperature and high frequency. **a**, Real and imaginary parts of K_{11} as a function of frequency. Orange indicates the high-frequency results, measured on a linear frequency scale, from which the loss tangent is computed. The inset shows the film loss tangent on a linear frequency scale in the gigahertz frequency regime, along with the linear fit. **b**, The ratio of K_{11} under an applied bias field (E_{bias}) to that at zero bias field (left-hand axis) and tunability (right-hand axis) of the $n = 6$ sample at several different frequencies in the microwave range. The inset shows the dielectric constant ratio as a function of frequency for several values of applied E_{bias}. **c**, Q_{11} (blue) and FOM (red) of the $n = 6$ sample at a bias field of 50 kV cm^{-1}, and the room-temperature FOM of a $Ba_xSr_{1-x}TiO_3$ film at 300 kV cm^{-1} (green) from ref. 30. The FOM of the $n = 6$ sample assumes that the loss tangent depends linearly on frequency and that the tunability is independent of frequency and is 20% at a bias of 50 kV cm^{-1}. Solid points are Q values averaged over a frequency range of 14.5 GHz.

polar nanoregions nucleate far below room temperature; at those temperatures they enhance both K_{11} and loss, resulting in the observed dielectric relaxation typical for relaxor ferroelectrics. Such behaviour could arise from the horizontal $(SrO)_2$ planes decoupling the in-plane polarization between the perovskite slabs that they separate, leading to nanopolar slabs. Commensurate $Sr_{n+1}Ti_nO_{3n+1}$ on $DyScO_3$ could thus be an embodiment of a new type of relaxor ferroelectric: one free of extrinsic disorder or the realization of a superparaelectric state. (There are also vertical $(SrO)_2$ planes. In contrast to the horizontal $(SrO)_2$ planes, however, the in-plane polarization of the $Sr_{n+1}Ti_nO_{3n+1}$ film is perpendicular to the vertical $(SrO)_2$ planes. From electrostatic arguments analogous to those for $BaTiO_3/SrTiO_3$ superlattices[31], the polarization should be continuous across the interface with the vertical $(SrO)_2$ planes.) The rapid decrease in the size of polar regions for $T > T_C$ is probably due to the lack of defects or the local nanostructure engineered into these materials, and is consistent with the exceptionally low dielectric loss and high FOM of the $n = 6$ film at room temperature in the microwave regime.

These results underscore the importance of both defect mitigation and our system that allows a ferroelectric instability to be tuned by means of atomic engineering without adding disorder. The high FOM already achieved extends the application of tunable dielectrics to significantly higher frequency. To allow this new material to be developed into practical devices, it is desirable to fabricate it on large-area substrates with low loss in the gigahertz frequency range. $DyScO_3$ substrates as large as 32 mm in diameter are currently grown by the Czochralski method[32]. These substrates could be scaled up, or the approach of making thick, relaxed $DyScO_3$ buffer layers (pseudo-substrates) on relevant low-loss substrates that are available in larger diameters could be pursued, as has been demonstrated for $PrScO_3$ (ref. 33). More broadly, however, a multitude of other oxide systems, whose performance in thin-film form is limited by point defects, could also be greatly enhanced with appropriate atomic engineering. Exploiting host systems that form planar defects more readily than point defects is clearly advantageous.

METHODS SUMMARY

We performed first-principles density-functional calculations using Kohn–Sham density function theory as implemented in VASP and using density-functional perturbation theory as implemented in Quantum ESPRESSO (Methods and Extended Data Fig. 1). We grew $Sr_{n+1}Ti_nO_{3n+1}$ ($n = 1$–6) thin films by reactive molecular-beam epitaxy, from elemental strontium and titanium sources at a substrate temperature of 750–780 °C in an oxidant background pressure ($O_2 + \sim 10\% O_3$) of 3×10^{-7} Torr (Methods). These films were characterized structurally by XRD (Extended Data Figs 2–4) and STEM. The paraelectric-to-ferroelectric transition was studied by SHG (Extended Data Fig. 5). The dielectric properties in the terahertz and infrared regime were measured by terahertz transmission and infrared reflectance (Methods and Extended Data Figs 6 and 7) and at microwave frequencies by on-wafer techniques with the use of interdigitated capacitors and coplanar waveguides (Methods and Extended Data Figs 8–10).

Online Content Any additional Methods, Extended Data display items and Source Data are available in the online version of the paper; references unique to these sections appear only in the online paper.

Received 18 April; accepted 19 August 2013.
Published online 16 October 2013.

1. Tagantsev, A. K., Sherman, V. O., Astafiev, K. F., Venkatesh, J. & Setter, N. Ferroelectric materials for microwave tunable applications. *J. Electroceram.* **11,** 5–66 (2003).
2. Kirchoefer, S. W. *et al.* Microwave properties of $Sr_{0.5}Ba_{0.5}TiO_3$ thin-film interdigitated capacitors. *Microw. Opt. Technol. Lett.* **18,** 168–171 (1998).
3. Gevorgian, S. S. & Kollberg, E. L. Do we really need ferroelectrics in paraelectric phase only in electrically controlled microwave devices? *IEEE Trans. Microw. Theory Tech.* **49,** 2117–2124 (2001).

4. Nakamura, T. *et al.* On the perovskite-related materials of high dielectric permittivity with small temperature dependence and low dielectric loss. *Ferroelectrics* **196,** 205–209 (1997).
5. Wise, P. L. *et al.* Structure–microwave property relations in $(Sr_xCa_{(1-x)})_{n+1}Ti_nO_{3n+1}$. *J. Eur. Ceram. Soc.* **21,** 1723–1726 (2001).
6. Andersson, S. & Wadsley, A. D. Crystallographic shear and diffusion paths in certain higher oxides of niobium, tungsten, molybdenum and titanium. *Nature* **211,** 581–583 (1966).
7. Anderson, J. S. *et al.* Point defects and extended defects in niobium oxides. *Nature* **243,** 81–83 (1973).
8. Tilley, R. J. D. Correlation between dielectric constant and defect structure of non-stoichiometric solids. *Nature* **269,** 229–231 (1977).
9. Tilley, R. J. D. An electron microscope study of perovskite-related oxides in the Sr-Ti-O system. *J. Solid State Chem.* **21,** 293–301 (1977).
10. Birol, T., Benedek, N. A. & Fennie, C. J. Interface control of emergent ferroic order in Ruddlesden–Popper $Sr_{n+1}Ti_nO_{3n+1}$. *Phys. Rev. Lett.* **107,** 257602 (2011).
11. Bao, P., Jackson, T. J., Wang, X. & Lancaster, M. J. Barium strontium titanate thin film varactors for room-temperature microwave device applications. *J. Phys. D Appl. Phys.* **41,** 063001 (2008).
12. Weiss, C. V. *et al.* Compositionally graded ferroelectric multilayers for frequency agile tunable devices. *J. Mater. Sci.* **44,** 5364–5374 (2009).
13. Pertsev, N. A., Tagantsev, A. K. & Setter, N. Phase transitions and strain-induced ferroelectricity in $SrTiO_3$ epitaxial thin films. *Phys. Rev. B* **61,** R825–R829 (2000).
14. Antons, A., Neaton, J. B., Rabe, K. M. & Vanderbilt, D. Tunability of the dielectric response of epitaxially strained $SrTiO_3$ from first principles. *Phys. Rev. B* **71,** 024102 (2005).
15. Li, Y. L. *et al.* Phase transitions and domain structures in strained pseudocubic (100) $SrTiO_3$ thin films. *Phys. Rev. B* **73,** 184112 (2006).
16. Haeni, J. H. *et al.* Room-temperature ferroelectricity in strained $SrTiO_3$. *Nature* **430,** 758–761 (2004).
17. Cole, M. W., Nothwang, W. D., Hubbard, C., Ngo, E. & Ervin, M. Low dielectric loss and enhanced tunability of $Ba_{0.6}Sr_{0.4}TiO_3$ based thin films via material compositional design and optimized film processing methods. *J. Appl. Phys.* **93,** 9218–9225 (2003).
18. Cole, M. W., Joshi, P. C. & Ervin, M. H. La doped $Ba_{1-x}Sr_xTiO_3$ thin films for tunable device applications. *J. Appl. Phys.* **89,** 6336–6340 (2001).
19. Babbitt, R. W., Koscica, T. E. & Drach, W. C. Planar microwave electrooptic phase shifters. *Microwave J.* **35,** 63–79 (1992).
20. Gevorgian, S., Carlsson, E., Wikborg, E. & Kollberg, E. Tunable microwave devices based on bulk and thin film ferroelectrics. *Integr. Ferroelectr.* **22,** 765–777 (1998).
21. Booth, J. C., Takeuchi, I. & Chang, K. S. Microwave-frequency loss and dispersion in ferroelectric $Ba_{0.3}Sr_{0.7}TiO_3$ thin films. *Appl. Phys. Lett.* **87,** 082908 (2005).
22. Ruddlesden, S. N. & Popper, P. New compounds of the K_2NiF_4 type. *Acta Crystallogr.* **10,** 538–540 (1957).
23. Ruddlesden, S. N. & Popper, P. The compound $Sr_3Ti_2O_7$ and its structure. *Acta Crystallogr.* **11,** 54–55 (1958).
24. Lee, J. & Arias, T. A. Structural phase transitions in Ruddlesden–Popper phases of strontium titanate: *ab initio* and modulated Ginzburg–Landau approaches. *Phys. Rev. B* **82,** 180104 (2010).
25. Xi, X. X. *et al.* Oxide thin films for tunable microwave devices. *J. Electroceram.* **4,** 393–405 (2000).
26. Lee, C.-H. *et al.* Effect of reduced dimensionality on the optical band gap of $SrTiO_3$. *Appl. Phys. Lett.* **102,** 122901 (2013).
27. Udayakumar, K. R. & Cormack, A. N. Structural aspects of phase-equilibria in the strontium–titanium–oxygen system. *J. Am. Ceram. Soc.* **71,** C469–C471 (1988).
28. Udayakumar, K. R. & Cormack, A. N. Non-stoichiometry in alkaline-earth excess alkaline-earth titanates. *J. Phys. Chem. Solids* **50,** 55–60 (1989).
29. Veličkov, B., Kahlenberg, V., Bertram, R. & Bernhagen, M. Crystal chemistry of $GdScO_3$, $DyScO_3$, $SmScO_3$ and $NdScO_3$. *Z. Kristallogr.* **222,** 466–473 (2007).
30. Houzet, G., Burgnies, L., Velu, G., Carru, J.-C. & Lippens, D. Dispersion and loss of ferroelectric $Ba_{0.5}Sr_{0.5}TiO_3$ thin films up to 110 GHz. *Appl. Phys. Lett.* **93,** 053507 (2008).
31. Neaton, J. B. & Rabe, K. M. Theory of polarization enhancement in epitaxial $BaTiO_3$/$SrTiO_3$ superlattices. *Appl. Phys. Lett.* **82,** 1586–1588 (2003).
32. Uecker, R. *et al.* Properties of rare-earth scandate single crystals (Re = Nd−Dy). *J. Cryst. Growth* **310,** 2649–2658 (2008).
33. Folkman, C. M., Das, R. R., Eom, C. B., Chen, Y. B. & Pan, X. Q. Single domain strain relaxed $PrScO_3$ template on miscut substrates. *Appl. Phys. Lett.* **89,** 221904 (2006).

Acknowledgements We acknowledge discussions with S. Trolier-McKinstry and C. A. Randall. Research was supported by Army Research Office (ARO) grants W911NF-09-1-0415 (for C.-H.L., Y.Z., J.A.M. and D.A.M.), W911NF-12-1-0437 (for Y.N., J.Z. and D.G.S.) and W911NF-10-1-0345 (for T.B., N.A.B. and C.J.F.); by the National Science Foundation (NSF) through Materials Research Science and Engineering Centers (MRSEC) grants DMR-0820404 (for R.H., E.V., X.X.X. and V.G.) and DMR-1120296 (for Y.K., J.D.B. and L.F.K.); by the Czech Science Foundation Project no. P204/12/1163 and the Czech Ministry of Education, Youth and Sports project LD12026 (for V.G., D.N. and S.K.); and by the Spanish Government and the European Union through grants EUI-ENIAC-2011-4349 and EUI-ENIAC 2010-04252 (for E.R.). C.-H.L. acknowledges stipend support from NSF grant DMR-0820404. J.A.M. acknowledges financial support from a National Defense Science & Engineering Graduate Fellowship. The dielectric and ferroelectric measurements in Fig. 3c were conducted at the Center for Nanophase Materials Sciences, which is sponsored at Oak Ridge National Laboratory by the Scientific User Facilities Division, Office of Basic Energy Sciences, US Department of Energy. This work was performed in part at the Cornell NanoScale Factory, a member of the National Nanotechnology Infrastructure Network, which is supported by the National Science Foundation (grant ECCS-0335765). This work made use of the electron microscopy facility of the Cornell Center for Materials Research (CCMR) with support from the NSF MRSEC programme (DMR 1120296) and NSF IMR-0417392.

Author Contributions The thin films were synthesized by C.-H.L. on single-crystal substrates grown by M.B. and R.U. The first-principles calculations were performed by T.B., N.A.B. and C.J.F. The films were characterized by microwave measurements by N.D.O., E.R., I.T. and J.C.B.; by SHG by R.H., E.V. and V.G.; by infrared reflectance and terahertz transmission by V.G., D.N. and S.K.; by STEM by Y.Z., J.A.M., L.F.K. and D.A.M.; by XRD by C.-H.L., Y.N., J.-S.Z., Y.K. and J.D.B.; and by capacitance by M.D.B. and S.K. X.X.X. helped analyse the data. C.-H.L., T.B., J.C.B., C.J.F. and D.G.S. wrote the manuscript. The study was conceived and guided by C.J.F. and D.G.S. All authors discussed results and commented on the manuscript.

Author Information Reprints and permissions information is available at www.nature.com/reprints. The authors declare no competing financial interests. Readers are welcome to comment on the online version of the paper. Correspondence and requests for materials should be addressed to D.G.S. (schlom@cornell.edu).

METHODS

Calculations of strained $Sr_{n+1}Ti_nO_{3n+1}$ Ruddlesden–Popper phases. The phonon frequencies in Fig. 1b are calculated from first principles using the direct method[34], which involves displacing ions and calculating the Hellmann–Feynman forces by a single self-consistent field calculation in Kohn–Sham density function theory (DFT) as implemented in VASP[35]. To reduce the computational cost and obtain high-quality results, symmetry-adapted modes[36] are used and the frequency of only the in-plane polar modes are calculated. (Details are presented in ref. 10.)

In Extended Data Fig. 1a, the ferroelectric soft-mode frequencies of Ruddlesden–Popper structures, calculated from first principles, are plotted for different strain values. The ferroelectric instability, which is reflected as an imaginary phonon frequency, emerges at a larger tensile strain for lower values of n. The emergence of ferroelectricity in $Sr_{n+1}Ti_nO_{3n+1}$ Ruddlesden–Popper phases can be understood by studying the coherence properties of the soft mode in bulk perovskite $SrTiO_3$ (ref. 10). From calculations of $SrTiO_3$ from first principles, we found that there is a finite critical thickness in the direction perpendicular to polarization, below which ferroelectricity is suppressed[10]. At the relatively modest strain values that $SrTiO_3$ becomes ferroelectric, the low-n Ruddlesden–Popper phases remain paraelectric because the perovskite slabs between the double SrO layers are too thin; hence, the coherence condition is not satisfied. The effect of biaxial tensile strain is to decrease the critical thickness, which leads to ferroelectricity emerging at lower n with increasing strain. This can also be seen in the phonon dispersions of $SrTiO_3$: dispersion of a phonon mode arises from the coupling of ionic motions in neighbouring cells, so a dispersionless phonon mode signals the absence of any coupling. If the branch stemming from the ferroelectric soft mode is dispersionless in a plane, there is no coupling between the ionic displacements in neighbouring cells in the same direction in real space, and the critical thickness required for ferroelectricity is zero. In this limit, a distortion confined to a single chain of atoms can decrease the energy, such as in $BaTiO_3$ (ref. 37).

In general, an estimation of the critical thickness can be made using the zero-frequency isosurface of the phonons (Extended Data Fig. 1b), which is directly obtained from phonon dispersion curves. (These dispersions are calculated using density-functional perturbation theory as implemented in Quantum ESPRESSO[38].) For unstrained $SrTiO_3$, the unstable wavevectors form three perpendicular disks at the zone centre. The product of π and the reciprocal of the radius of these disks is a first-order approximation to the critical thickness for ferroelectric or antiferroelectric order[10]. (Note that even though DFT predicts a ferroelectric instability in unstrained $SrTiO_3$, it is suppressed by quantum fluctuations. The result is the occurrence of quantum paraelectric behaviour.) Tensile biaxial strain increases the radii of two of these disks, which correspond to in-plane polarization. At sufficient strain, the disks with almost perfectly flat isosurfaces extend from zone centre to zone boundary, and hence into the next Brillouin zone. In this limit the effective radii are infinite, the phonon branch is dispersionless, and the critical thickness vanishes (See Extended Data Fig. 1b, from left to right.)

In summary, DFT results show that one can tune the critical thickness required for the emergence of a ferroelectric state using biaxial strain. In addition, the ferroelectric phase transition temperature and dielectric properties under a certain fixed strain state can be tuned by the number of $SrTiO_3$ perovskite layers between the double SrO layers, that is, by n. The calculations also indicated that $Sr_{n+1}Ti_nO_{3n+1}$ phases commensurately strained to (110) $DyScO_3$ should be ferroelectric for $n \geq 3$ (Extended Data Fig. 1a)[10]. (Even though $n = 2$ has an instability, the energy gain of the ferroelectric phase is so little that the quantum fluctuations of the nuclei are expected to suppress any ferroelectric order[10].)

To find the energy difference between the polar and nonpolar states presented in Fig. 1b, we broke the symmetry of the high-symmetry paraelectric structure and relaxed the ionic positions to obtain the minimum energy in the polar space group. These relaxations are performed with fixed biaxial strain boundary conditions; that is, the in-plane lattice constants are fixed but the out-of-plane spacing is relaxed. The maximum energy gain is obtained for polarization along the [110] direction, as can be seen in Fig. 1c as well. The energy surfaces in Fig. 1c are obtained by freezing in different amplitudes of the polar distortion along in-plane directions and performing a DFT calculation in these structures. For $n = 1$ the polar distortion pattern, which involves not only the displacement of the titanium cations but also that of strontium and oxygen ions, is obtained from phonon calculations in the paraelectric structure. The force constants matrix eigenvector that has the lowest eigenvalue and that transforms as the in-plane polar irreducible representation E_u is used as the distortion pattern. For $n > 1$, which are the compounds that have polar distortions in the ground state, a different procedure is used: instead of performing the same procedure, the polar distortion patterns are obtained by taking the difference between the paraelectric high-symmetry structure and the polar structure (which is obtained by relaxing the ionic positions under fixed biaxial strain boundary conditions). This procedure gives more relevant results because it takes into account possible mixing of the soft mode with low-lying hard modes. This mixing becomes more important for larger values of n because the unit cell gets larger and other polar modes with low frequency emerge.

MBE growth of strained $Sr_{n+1}Ti_nO_{3n+1}$ Ruddlesden–Popper phases. The $Sr_{n+1}Ti_nO_{3n+1}$ ($n = 1$–6) films were grown in Veeco GEN10 and 930 oxide molecular-beam epitaxy systems. Molecular beams of strontium and titanium were generated by using a low-temperature effusion cell and a Ti-Ball[39], respectively. The fluxes of both elements were roughly calibrated with a quartz crystal microbalance. A more accurate flux calibration was then achieved by using shuttered reflection high-energy electron diffraction (RHEED) intensity oscillations[40]. The ratio between strontium and titanium doses was set to 1:1 by adjusting their durations until the maxima and minima of the shuttered RHEED oscillations neither grew nor diminished in intensity[40]. Once this ratio was correct, the absolute quantity of atoms deposited in each shuttered dose was adjusted to one monolayer of SrO and one monolayer of TiO_2 by monitoring for and avoiding a beat frequency in the shuttered RHEED oscillation envelope[40]. To grow $Sr_{n+1}Ti_nO_{3n+1}$ phases, both the stoichiometry and each monolayer absolute dose cannot be incorrect by more than about 1%. Each of the members in this series has different sequences of SrO and TiO_2 layers. The strontium and titanium molecular beams were shuttered to match the layering sequence of the desired (001)-oriented $Sr_{n+1}Ti_nO_{3n+1}$ phases.

(110) $DyScO_3$ and (110) $GdScO_3$ substrates were chosen to provide biaxial tensile strain to the $Sr_{n+1}Ti_nO_{3n+1}$ films. The lattice mismatch of the whole series of films to the substrates decreases with n: 1.8% for $n = 1$ and 1.1% for $n = \infty$ on $DyScO_3$; 2.3% for $n = 1$ and 1.6% for $n = \infty$ on $GdScO_3$. The films grown on $DyScO_3$ were roughly 500 Å thick, whereas those grown on $GdScO_3$ were 250 Å thick to avoid strain relaxation. The substrate temperature was held at 750–780 °C in an oxidant background pressure (O_2 + ~10% O_3) of 3×10^{-7} Torr during growth. This oxidant background pressure was maintained after growth until the substrate had cooled to below 200 °C.

Determination of dielectric properties in terahertz and infrared regions. Infrared reflectance measurements with near-normal-incidence polarized light were made from 10 to 300 K with a Bruker IFS 113v Fourier-transform infrared spectrometer equipped with a helium-cooled (1.5 K) silicon bolometer. A $Sr_7Ti_6O_{19}/DyScO_3$ sample 50 nm thick and a bare $DyScO_3$ substrate were measured in two polarizations ($\boldsymbol{E}||[001]$ and $\boldsymbol{E}||[1\bar{1}0]$ with respect to the (110) $DyScO_3$ substrate) under the same conditions on cooling to 10 K in an Optistat CF cryostat (Oxford Instruments). The thick polyethylene windows used in this measurement were transparent to infrared only up to 650 cm^{-1}. The terahertz measurements were performed with a custom-made terahertz time-domain spectrometer based on a Ti:sapphire femtosecond laser. Linearly polarized terahertz probing pulses were generated by an interdigitated photoconducting GaAs switch and detected by electro-optic sampling with a (110) ZnTe crystal 1 mm thick. The in-plane complex dielectric response of the thin films was calculated from the complex terahertz transmittance spectra measured in an Optistat CF cryostat[41].

The dielectric response of the bare substrate was evaluated by fitting the infrared reflectivity spectra

$$R(\omega) = \left| \frac{\sqrt{\varepsilon^*(\omega)} - 1}{\sqrt{\varepsilon^*(\omega)} + 1} \right|^2 \quad (1)$$

to a factorized form of the complex permittivity

$$\varepsilon^*(\omega) = \varepsilon_\infty \prod_j \frac{\omega_{LO_j}^2 - \omega^2 + i\omega\gamma_{LO_j}}{\omega_{TO_j}^2 - \omega^2 + i\omega\gamma_{TO_j}} \quad (2)$$

where ω_{TO_j} and ω_{LO_j} are the frequencies of jth transverse optic (TO) and longitudinal optic (LO) polar modes, respectively, and γ_{TO_j} and γ_{LO_j} are their damping constants. ε_∞ is the high-frequency (electronic) contribution to the permittivity.

The obtained parameters (ω_{TO_j}, ω_{LO_j}, γ_{TO_j}, γ_{LO_j} and ε_∞) were used to fit the infrared reflectance spectra of the $Sr_7Ti_6O_{19}/DyScO_3$ sample (Extended Data Fig. 6a) as a two-slab system. The dielectric function of the $Sr_7Ti_6O_{19}$ film was assumed to have the form of a sum of n independent damped harmonic oscillators, which represent the in-plane polarized TO phonon modes of the film and can be written as

$$\varepsilon^*(\omega) = \varepsilon_\infty + \sum_{j=1}^{n} \frac{\Delta\varepsilon_j \omega_{TO_j}^2}{\omega_{TO_j}^2 - \omega^2 + i\omega\gamma_{TO_j}} \quad (3)$$

where $\Delta\varepsilon_j$ is the dielectric strength of the jth mode. The real and imaginary parts of the complex dielectric constant $K_{11} = \varepsilon^*/\varepsilon_0$, where ε_0 is the permittivity of free space (Extended Data Fig. 6b) and the phonon parameters (Extended Data Fig. 7b), were obtained from fitting the reflectance spectra. Terahertz spectra taken below 275 K (Extended Data Fig. 6b) reveal a broad dielectric relaxation below the soft mode, which is the so-called central mode. This central mode was fitted with an

overdamped oscillator ($\gamma_{TO} > \omega_{TO}$). The relaxation frequency corresponding to $\omega^2_{CM}/\gamma_{CM}$ in the dielectric loss spectra is plotted in Extended Data Fig. 7b.

The static permittivity $\varepsilon'(0)$ obtained from infrared spectra is given by the sum of all phonon contributions and the high-frequency permittivity:

$$\varepsilon'(0) = \sum \Delta\varepsilon_j + \varepsilon_\infty \quad (4)$$

A peak in the static dielectric constant arises at about 225 K (Extended Data Fig. 7a), simultaneously with the appearance of a new polar phonon near 125 cm^{-1} in the infrared spectra (Extended Data Fig. 7b). The split polar phonon mode is evidence for a change in the crystal structure of the polar clusters at 225 K; that is, ~40 K above the peak in the dielectric constant measured at 1 MHz (see Fig. 3a).

We stress that no central mode was observed in room-temperature infrared and terahertz spectra (pink curve in Extended Data Fig. 6b). The dielectric increment is solely coming from the contribution of the low-frequency phonon (soft mode) at room temperature (Extended Data Fig. 7a); that is, no contribution from polar nanoregions is observed. This observation is in agreement with an analysis of the frequency dependence of the dielectric constant measured in the microwave range (Extended Data Fig. 9a). These results are consistent with a relatively homogenous, defect-free material without polar nanoregions. For this reason microwave dielectric losses are low and the FOM is exceptionally high.

In addition to an $n = 6/DyScO_3$ film, we also measured $Sr_{n+1}Ti_nO_{3n+1}$ ($n = 1$–5) thin films grown on $DyScO_3$. These data and a comparison with the infrared spectra of bulk $Sr_{n+1}Ti_nO_{3n+1}$ ceramics[42,43] are available from the authors. In brief, the lowest-frequency phonon (soft mode) always shows anomalies and splits near the T_C of the $Sr_{n+1}Ti_nO_{3n+1}$ ($n \geq 3$) thin films on $DyScO_3$, whereas the soft mode of bulk $Sr_{n+1}Ti_nO_{3n+1}$ shows incipient ferroelectric behaviour; that is, softening on cooling and saturation at low temperatures[42,43]. In addition, the phonon contributions to the dielectric constant near T_C of the $Sr_{n+1}Ti_nO_{3n+1}$ ($n \geq 3$) thin films on $DyScO_3$ are always lower than the experimental radiofrequency dielectric constants. This provides evidence of the existence of a central mode below phonon frequencies and a crossover from displacive to order–disorder ferroelectric phase transitions in these phases.

Determination of dielectric properties at microwave frequencies. The broadband dielectric properties of the thin-film samples were obtained over a frequency range of 1 kHz to 125 GHz from measurements of an ensemble of planar devices patterned onto the film surface. The devices were lithographically patterned, followed by electron-beam evaporation of a titanium adhesion layer 10 nm thick followed by a gold electrode layer 750 nm thick. Lift-off was then performed to complete the structures. Below 100 MHz, the admittance of interdigitated capacitors (IDCs) of different lengths was measured with a combination of an LCR meter (1 kHz to 1 MHz) and a radiofrequency vector network analyser (1–200 MHz). From 100 MHz to 125 GHz, the complex scattering (*S*-) parameters of distributed coplanar waveguide (CPW) transmission lines were measured with a variety of vector network analysers. The CPW cross-section had a 60-μm centre conductor, 20-μm gaps and 200-μm-wide ground planes. The active lengths ranged from 0.420 mm to 5.933 mm. In cross-section, the IDCs had 60-μm finger widths separated by 20-μm gaps with 200-μm ground planes, spaced 50-μm from the fingers. The interdigitated finger overlaps, or active lengths of the IDCs, ranged from 0.100 mm to 2.900 mm. The device layout and cross-sections are shown in Extended Data Fig. 8a, b, respectively. On-wafer error correction was employed for all measurements with a custom calibration standard fabricated on a reference wafer. Such calibrations are based on the multiline through-reflect-line approach[44,45] and are unique in that a single set of standards defines a reference impedance over a very broad frequency range[46,47].

From the IDC measurements, the admittance per unit length was obtained by a linear regression of the admittance against active length. The CPW measurements were analysed with an *S*-parameter optimization technique and yielded the frequency-dependent distributed circuit parameters (resistance, inductance, capacitance and conductance per unit length), for both thin-film samples and bare substrates[47]. The frequency-dependent capacitance and conductance per unit length obtained were then converted to the in-plane dielectric constant of the $Sr_{n+1}Ti_nO_{3n+1}$ films (K_{11}) with finite-element simulations for the relevant device cross-sections. Measurements were made in the range 40–298 K with a variable-temperature microwave probe station. Electric-field-biased measurements were made (for bias voltages up to 100 V over the frequency range 0.1–40 GHz) by using external bias tees.

To supplement the low-frequency dielectric constant measured as a function of temperature shown in Fig. 3a for different samples, and the tunable properties at room temperature for $n = 6/DyScO_3$ shown in Fig. 4, measurements of the frequency-dependent complex dielectric constant from 1 kHz to 40 GHz at various temperatures between 40 and 298 K were also obtained, for zero electric field bias. Results are shown for the real part of the dielectric constant K_{11} of the $n = 6/DyScO_3$ sample in Extended Data Fig. 9a, b, for temperatures above and below the experimentally determined T_C, respectively.

On the basis of the relaxor-like behaviour observed in Fig. 3a, we fitted the frequency-dependent complex permittivity at fixed temperature T to the model of ref. 48, which quantifies the contribution to the permittivity of a collection of polar clusters that can have a distribution of sizes. This approach assigns a relaxation time τ_1 with dielectric increment $\Delta\varepsilon_1$ to each polar cluster and assumes an exponential distribution of cluster sizes. The frequency-dependent dielectric constant $K_{11} = \varepsilon^*/\varepsilon_0$ is then calculated from the following expression for the frequency-dependent permittivity:

$$\varepsilon^*(\omega) = \varepsilon_\infty + m\Delta\varepsilon_1 \int_0^\infty \frac{e^{-mx}}{1 + i\omega\tau_c e^x} dx \quad (5)$$

where ε_∞ includes permittivity contributions at frequencies above the microwave range, $\Delta\varepsilon_1$ is the dielectric permittivity increment of the polar clusters, τ_c is the cut-off relaxation time of the smallest polar clusters, and $m = k_B T/E_0$; k_B is the Boltzmann constant and E_0 is an activation energy that characterizes the width of the polar cluster distribution. A small value for E_0 represents a uniform distribution, whereas larger E_0 values characterize an increasingly larger distribution of cluster sizes.

The frequency-dependent complex dielectric constant at fixed temperature T, shown in Extended Data Fig. 9a, b, was fitted to equation (5) with four adjustable parameters: ε_∞, $\Delta\varepsilon_1$, τ_c and E_0. We initially fitted the data at each temperature allowing all four parameters to vary, and discovered that adequate fits could be obtained only with a relatively narrow range of values for the relaxation time of the smallest polar cluster τ_c ($\sim 10^{-13}$ s) and high-frequency permittivity ($\varepsilon_\infty/\varepsilon_0 \sim 400$). We then re-fitted the data at all temperatures with constrained values for τ_c and ε_∞, allowing $\Delta\varepsilon_1$ and E_0 to vary, and obtained the fits shown in Extended Data Fig. 9a, b. The resultant temperature-dependent $\Delta\varepsilon_1(T)$ and $E_0(T)$ are shown in Extended Data Fig. 10a, b. Note that a constant $\varepsilon_\infty(T)$ is consistent with the weak temperature dependence observed in the infrared results (Extended Data Fig. 6b).

The agreement between the measured data and fits to equation (5) confirms the relaxation dynamics of the dielectric response of these novel tunable dielectrics. The temperature dependence of $\Delta\varepsilon_1(T)$ represents the frequency-independent response of the static permittivity and can be used to define the T_C of the material. The temperature dependence of $E_0(T)$ quantifies the growth of the distribution of polar clusters, which peaks at T_C and remains relatively large for temperatures below T_C. Thus, the losses in these materials are due to the distribution of finite-sized polar clusters and show that to obtain low-loss materials it is necessary to control both the size and the distribution of polar clusters. In general, maximum tuning is observed near the T_C of the material, which leads to competing requirements for high tunability and low loss. Examination of Extended Data Fig. 10a, b shows that for $n = 6/DyScO_3$, E_0 (the distribution of polar regions) drops precipitously for $T > T_C$, resulting in low loss at room temperature, where some dielectric increment (tuning) due to the ferroelectric phase transition still remains. This rapid decrease in E_0 for $T > T_C$ is probably due to the lack of defects or the local nanostructure engineered into these materials, and is the key to obtaining a high FOM at microwave frequencies.

E_0 decreases below T_C because the size distribution of the polar regions decreases in the ferroelectric phase. Polar nanoregions that formed above T_C suddenly transform into ferroelectric domains during cooling below T_C. The size of the domains is small, a result of the film thickness being only 50 nm and the domains' size following Kittel's scaling law[49]. If we assume that the ferroelectric domain size is comparable to the film thickness, the domains are still one order of magnitude larger than polar nanoclusters in relaxor ferroelectrics, which do not exceed ~60 Å in diameter[50].

34. Kunc, K. & Martin, R. M. *Ab initio* determination of static, dynamic and dielectric properties of semiconductors. *Physica B* **117/118,** 511–516 (1983).
35. Kresse, G. & Hafner, J. *Ab initio* molecular dynamics for liquid metals. *Phys. Rev. B* **47,** 558–561 (1993).
36. Perez-Mato, J. M., Orobengoa, D. & Aroyo, M. I. Mode crystallography of distorted structures. *Acta Crystallogr. A* **66,** 558–590 (2010).
37. Ghosez, P., Gonze, X. & Michenaud, J. P. *Ab initio* phonon dispersion curves and interatomic force constants of barium titanate. *Ferroelectrics* **206,** 205–217 (1998).
38. Giannozzi, P. *et al.* Quantum ESPRESSO: a modular and open-source software project for quantum simulations of materials. *J. Phys. Condens. Matter* **21,** 395502 (2009).
39. Theis, C. D. & Schlom, D. G. Cheap and stable titanium source for use in oxide molecular beam epitaxy systems. *J. Vac. Sci. Technol. A* **14,** 2677–2679 (1996).
40. Haeni, J. H., Theis, C. D. & Schlom, D. G. RHEED intensity oscillations for the stoichiometric growth of $SrTiO_3$ thin films by reactive molecular beam epitaxy. *J. Electroceram.* **4,** 385–391 (2000).
41. Kadlec, C. *et al.* High tunability of the soft mode in strained $SrTiO_3/DyScO_3$ multilayers. *J. Phys. Condens. Matter* **21,** 115902 (2009).

42. Noujni, D. *et al.* Temperature dependence of microwave and THz dielectric response in $Sr_{n+1}Ti_nO_{3n+1}$ (n=1–4). *Integr. Ferroelectr.* **62,** 199–203 (2004).
43. Kamba, S. *et al.* Composition dependence of the lattice vibrations in $Sr_{n+1}Ti_nO_{3n+1}$ Ruddlesden–Popper homologous series. *J. Eur. Ceram. Soc.* **23,** 2639–2645 (2003).
44. Marks, R. B. A multiline method of network analyzer calibration. *IEEE Trans. Microw. Theory Tech.* **39,** 1205–1215 (1991).
45. Williams, D. F., Wang, J. C. M. & Arz, U. An optimal vector-network-analyzer calibration algorithm. *IEEE Trans. Microw. Theory Tech.* **51,** 2391–2401 (2003).
46. Orloff, N. D. *et al.* A compact variable-temperature broadband series-resistor calibration. *IEEE Trans. Microw. Theory Tech.* **59,** 188–195 (2011).
47. Orloff, N., Mateu, J., Murakami, M., Takeuchi, I. & Booth, J. C. in *Proc. IEEE MTT-S Int. Microwave Symp.* 1177–1180 (IEEE Publishing, 2007).
48. Lu, Z. G. & Calvarin, G. Frequency dependence of the complex dielectric permittivity of ferroelectric relaxor. *Phys. Rev. B* **51,** 2694–2702 (1995).
49. Catalan, G., Seidel, J., Ramesh, R. & Scott, J. F. Domain wall nanoelectronics. *Rev. Mod. Phys.* **84,** 119–156 (2012).
50. Xu, G., Shirane, G., Copley, J. R. D. & Gehring, P. M. Neutron elastic diffuse scattering study of $Pb(Mg_{1/3}Nb_{2/3})O_3$. *Phys. Rev. B* **69,** 064112 (2004).

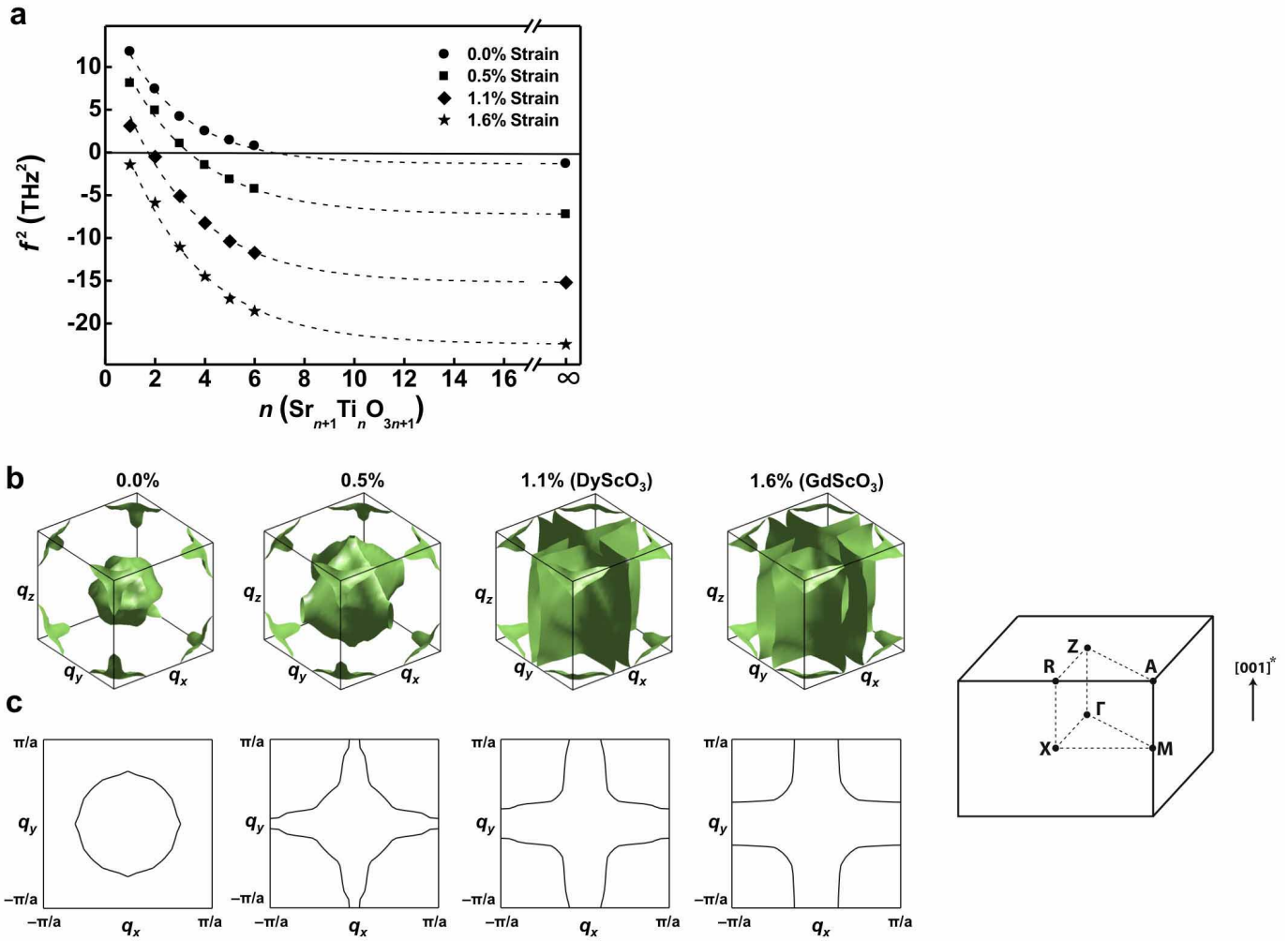

Extended Data Figure 1 | First-principles calculations showing the emergence of a ferroelectric instability in $Sr_{n+1}Ti_nO_{3n+1}$ phases. **a**, In-plane polar soft-mode (lowest-frequency transverse optical phonon) square of frequency against index n. Strain values are given with respect to the lattice constant of $SrTiO_3$. The dashed lines are fits to exponentials. **b**, Zero-frequency isosurface of the soft-mode phonon of $SrTiO_3$ in the first Brillouin zone. From left to right: cubic $SrTiO_3$ under no strain, 0.5%, 1.1% and 1.6% tensile biaxial strain. The last two correspond to (110) $DyScO_3$ and (110) $GdScO_3$ substrates, respectively; the small anisotropy of the substrate surfaces are taken into account in the calculations. The high-symmetry points are provided for the simple tetragonal cell. **c**, (001)* cuts through the surfaces in **b** at the $q_z = 0$ plane.

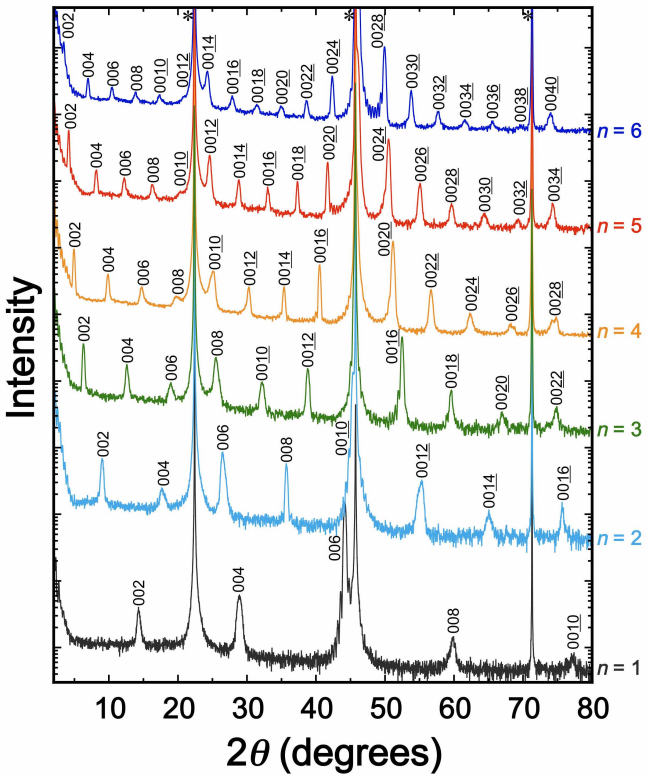

Extended Data Figure 2 | θ–2θ XRD scans of the epitaxial $Sr_{n+1}Ti_nO_{3n+1}$ ($n = 1$–6) films grown on (110) $GdScO_3$. Substrates peaks are labelled with an asterisk, and the plots are offset for clarity.

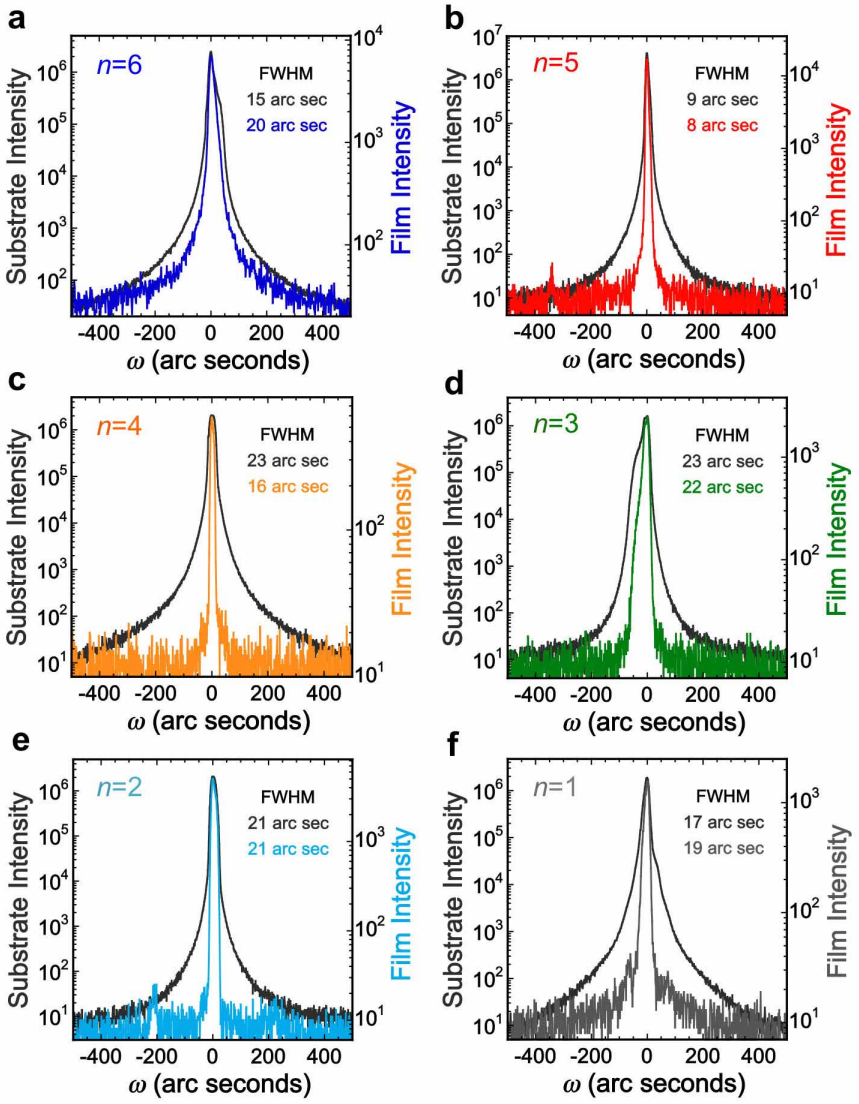

Extended Data Figure 3 | Superimposed XRD rocking curves of selected film peaks of the $Sr_{n+1}Ti_nO_{3n+1}$ films and the underlying 220 $DyScO_3$ substrate peaks. **a**, $n = 6$ (00$\underline{26}$ peak, blue). **b**, $n = 5$ (00$\underline{22}$ peak, red). **c**, $n = 4$ (00$\underline{20}$ peak, orange). **d**, $n = 3$ (00$\underline{14}$ peak, green). **e**, $n = 2$ (00$\underline{10}$ peak, light blue). **f**, $n = 1$ (006 peak, grey). The full-width at half-maximum (FWHM) of the substrate and film peaks are given.

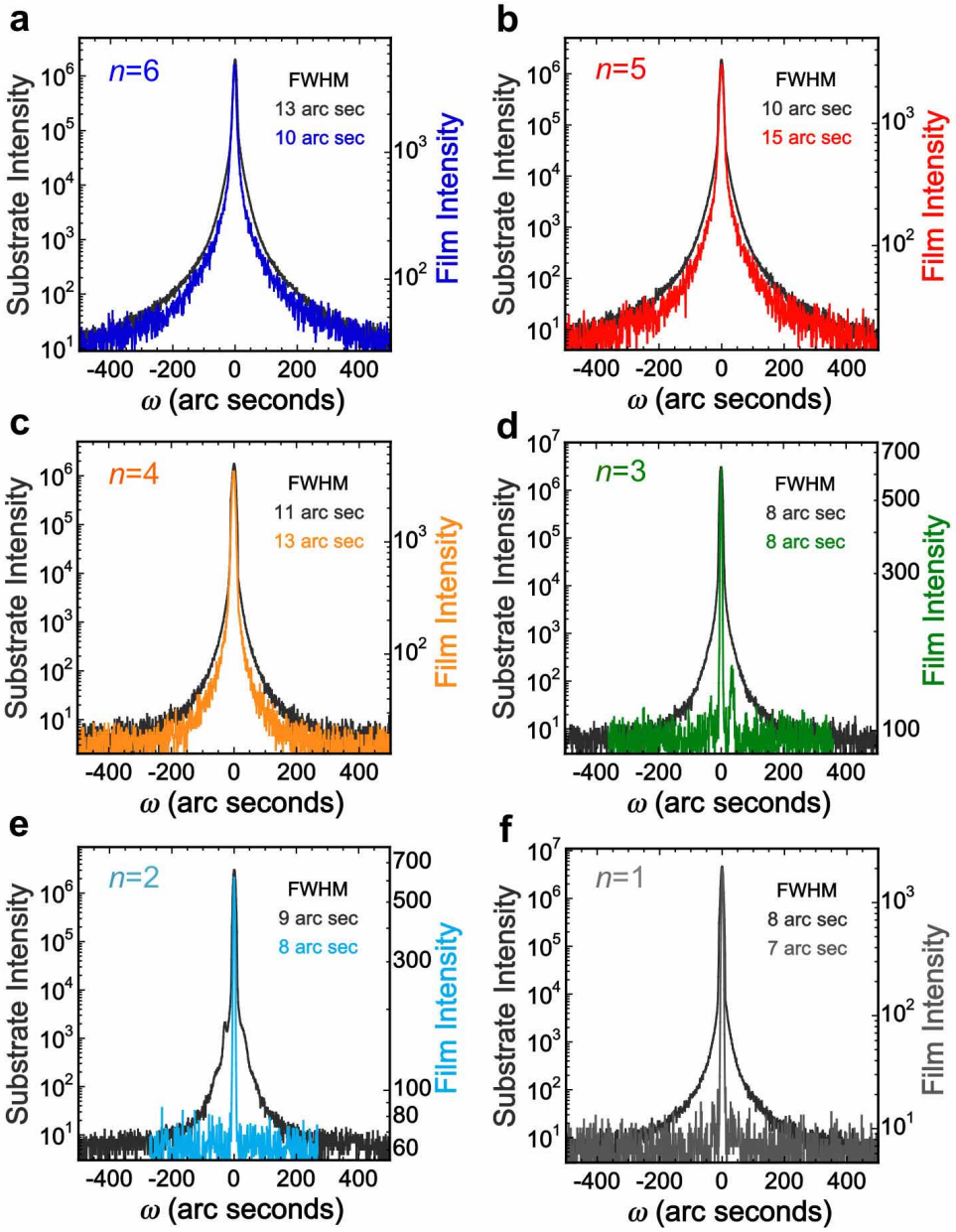

Extended Data Figure 4 | Superimposed XRD rocking curves of selected film peaks of the $Sr_{n+1}Ti_nO_{3n+1}$ films and the underlying 220 $GdScO_3$ substrate peaks. **a**, $n = 6$ (00$\underline{26}$ peak, blue). **b**, $n = 5$ (00$\underline{22}$ peak, red). **c**, $n = 4$ (00$\underline{18}$ peak, orange). **d**, $n = 3$ (00$\underline{16}$ peak, green). **e**, $n = 2$ (008 peak, light blue). **f**, $n = 1$ (006 peak, grey). The FWHM of the substrate and film peaks are given.

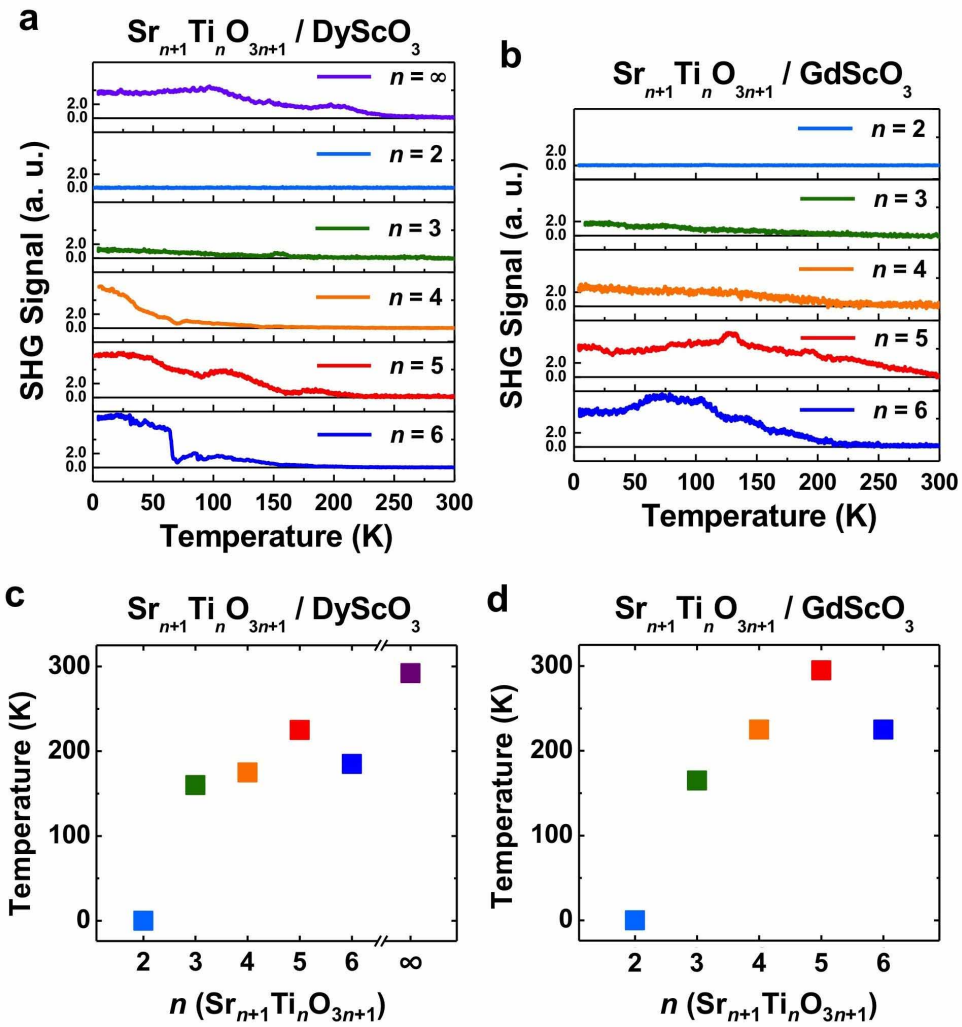

Extended Data Figure 5 | Nonlinear optical SHG temperature scans of $Sr_{n+1}Ti_nO_{3n+1}$ ($n = 2$–6 and $n = \infty$) films. **a**, Films grown on (110) $DyScO_3$. **b**, Films grown on (110) $GdScO_3$ substrates. The SHG signal for each temperature scan was normalized with the laser input power, where the SHG signal axis for each scan shows normalized tick labels at 0 and 2 to compare the signal strength between samples. **c**, **d**, The paraelectric-to-ferroelectric transition temperatures (T_C) measured by SHG were determined as the point where the SHG signal vanishes to zero and are shown for $DyScO_3$ (**c**) and $GdScO_3$ (**d**). The error bars are ±10 K, about the height of each square symbol in **c** and **d**.

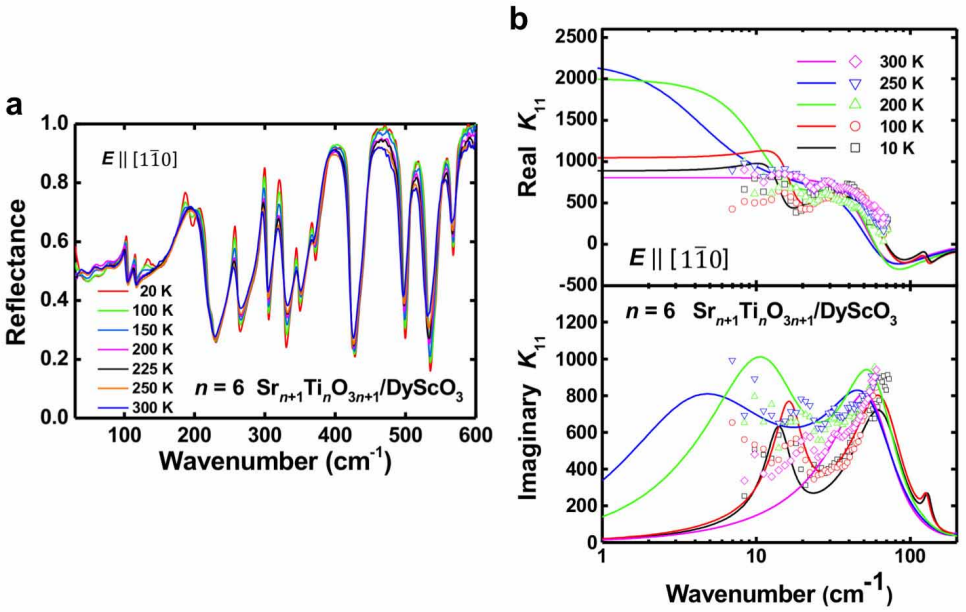

Extended Data Figure 6 | Real and imaginary parts of the in-plane complex dielectric constant (K_{11}) of the $Sr_7Ti_6O_{19}/DyScO_3$ sample at terahertz frequencies. **a**, Infrared reflectance spectra of the $Sr_7Ti_6O_{19}/DyScO_3$ sample (E || [1$\bar{1}$0]). **b**, Real and imaginary parts of the measured complex terahertz dielectric spectra (hollow symbols) overlapped with fittings (lines) to the infrared and terahertz spectra.

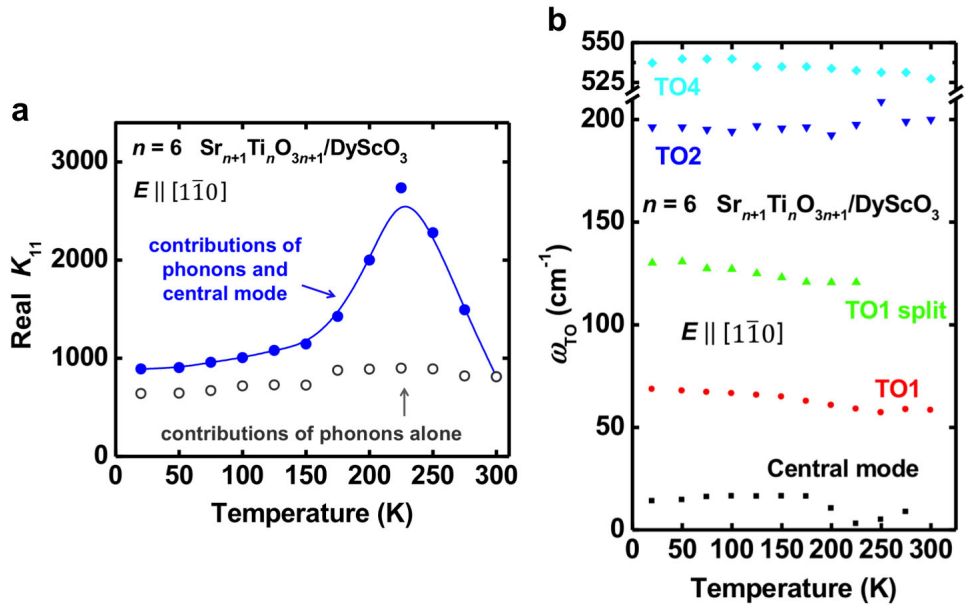

Extended Data Figure 7 | Analysis of the contributions to K_{11} from phonons and the central mode. **a**, Temperature dependence of the real part of the static dielectric constant (K_{11}) of the $n = 6/DyScO_3$ sample. Grey hollow dots show the contribution of solely the low-frequency phonons (soft mode) to K_{11} calculated from infrared spectra. The blue curve shows contributions from both low-frequency phonons and polar nanoregions (central mode) calculated from infrared and terahertz spectra. **b**, Temperature dependence of the polar phonons and the central-mode frequencies.

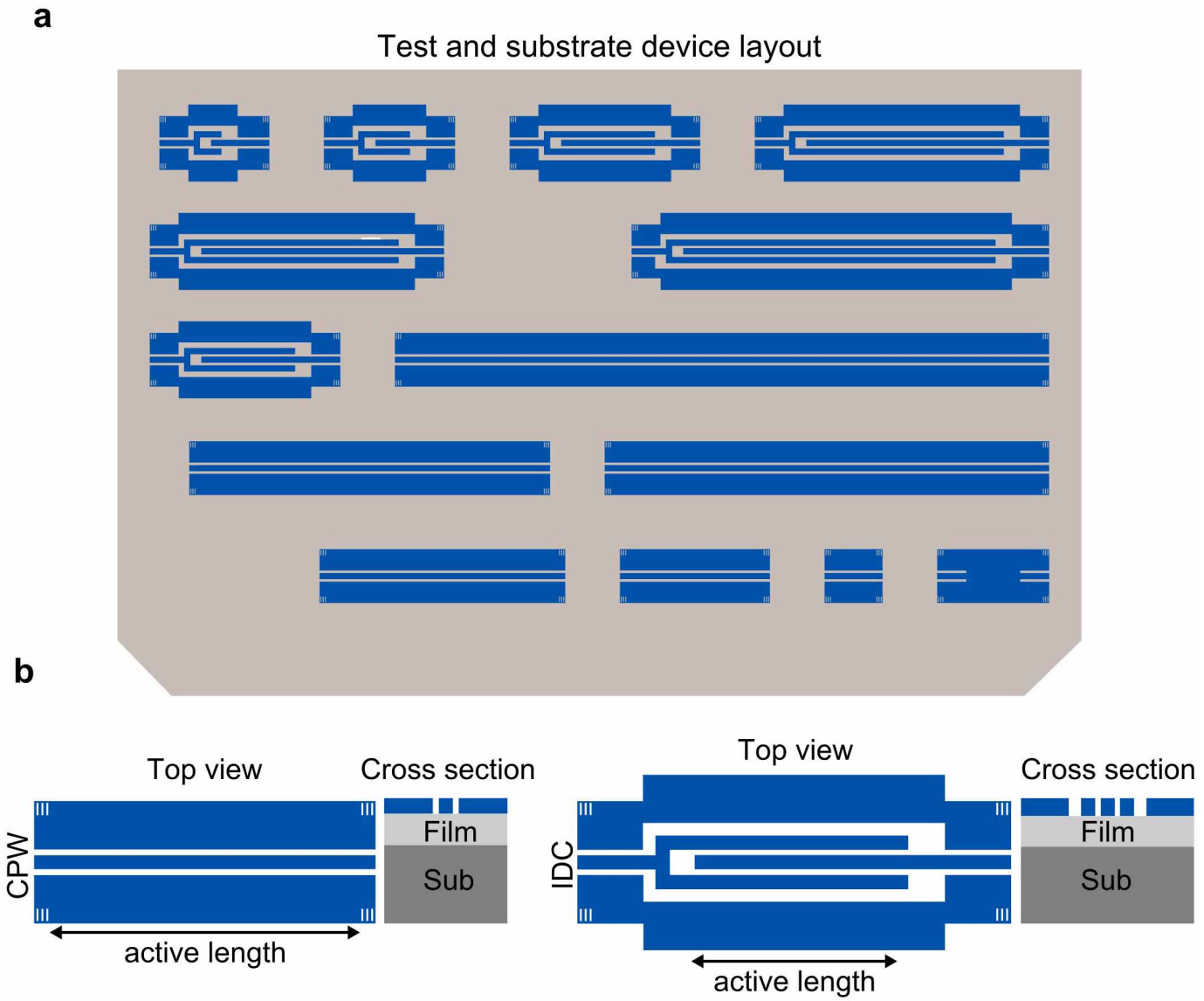

Extended Data Figure 8 | Geometry of the coplanar waveguide and interdigitated capacitor device structures measured. **a**, Diagram of the test and substrate device layout for the $Sr_{n+1}Ti_nO_{3n+1}$ thin films and $DyScO_3$ and $GdScO_3$ substrates with coplanar waveguides (CPWs) and interdigitated capacitor (IDC) devices. The substrate is shown in light grey, and the 760-nm-thick Ti/Au electrodes in blue. **b**, Top views and cross-sections of the CPW and IDC device geometry. The cross-section thicknesses are not to scale.

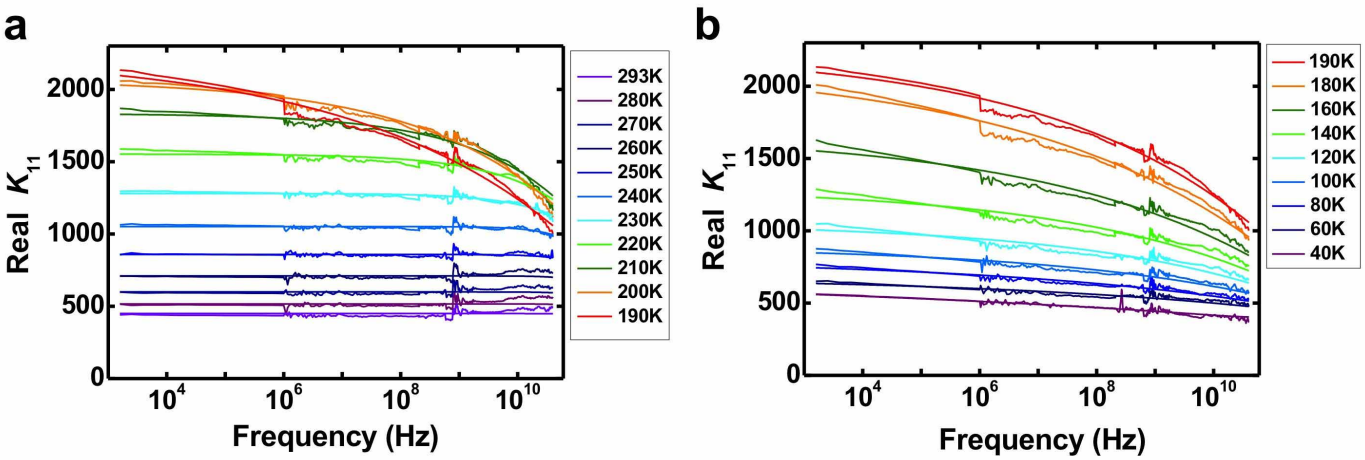

Extended Data Figure 9 | Frequency dependence of the real part of the complex dielectric constant of the $n = 6/DyScO_3$ sample at microwave frequencies for various temperatures, *T*. **a**, $T > T_C$. **b**, $T < T_C$. Solid lines denote fits based on a model that includes effects due to a distribution of relaxation times in the system. Although only the real part of the complex dielectric constant is shown, both real and imaginary parts are included in the fits.

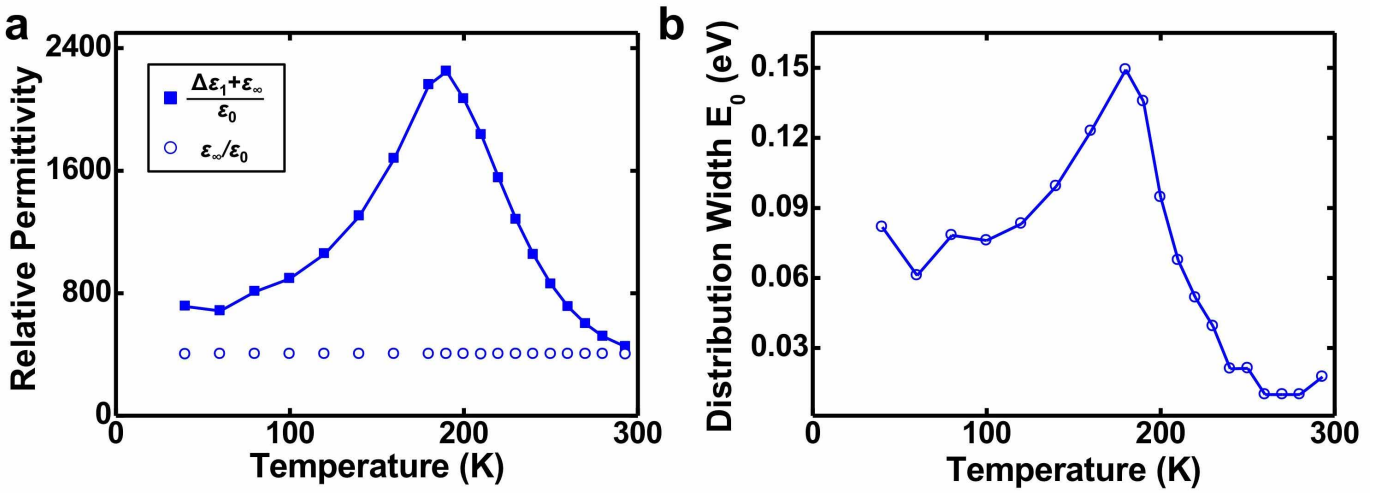

Extended Data Figure 10 | Temperature dependence of fit parameters for the results shown in Extended Data Fig. 9. **a**, Static and high-frequency dielectric constants. **b**, The width of the distribution of relaxation times. The value for the relaxation time of the smallest polar clusters is fixed at $\tau = 10^{-13}$ s.